

Magnetization and domain structure of bcc Fe₈₁Ni₁₉/Co (001) superlatticesR. Bručas, H. Hafermann, M. I. Katsnelson, I. L. Soroka, O. Eriksson, and B. Hjörvarsson
Department of Physics, Uppsala University, P. O. Box 530, 751 21 Uppsala, Sweden

(Received 3 October 2003; published 12 February 2004)

Dense stripe domains were observed for a Fe₈₁Ni₁₉/Co superlattice grown on a MgO(100) single crystal substrate using dc magnetron sputtering. The stripe domain period exhibits nonreversible changes with the magnetic field, as determined by magnetic force microscopy. We present a simple theoretical model for this system and calculate the magnetization and domain period as functions of the applied field by minimizing the total energy. For this purpose, an expression for the domain wall energy and wall width for arbitrary angles and one for the magnetostatic energy are derived. The model correctly predicts a decreasing domain period with the increasing applied field. At larger magnetic fields a transition to “chaotic” two-dimensional stripe patterns is observed and a qualitative discussion of this phenomenon is given.

DOI: 10.1103/PhysRevB.69.064411

PACS number(s): 75.60.-d, 75.70.-i, 75.75.+a, 75.10.-b

I. INTRODUCTION

Ferromagnetic multilayered thin films are a subject of growing interest in recent years. It is motivated to a large extent by industrial importance of these films, due to possible applications in ultrahigh magnetic and magneto-optic data storage devices and sensors.¹⁻⁵ To be able to tailor the magnetocrystalline anisotropy, and thereby allow both perpendicular and parallel magnetization with respect to the film surface, is especially important for these aims. In this context, investigations of the magnetic domain structure are of great interest, because they allow to extract information about magnetization and anisotropy. Furthermore, a full understanding of the magnetic domain configurations will provide fundamental insights as well as help to achieve technically based objectives, since the magnetization reversal mechanism is closely related to the domain structures.

Magnetic domains and domain walls can be probed by Lorentz microscopy,⁶ electron holography,⁷ scanning electron microscopy with polarization analysis (SEMPA),⁸ Kerr microscopy,⁹ magnetic transmission x-ray microscopy (MTXM),¹⁰ and magnetic force microscopy (MFM).¹¹⁻¹⁵ Techniques which allow imaging the magnetic domains in the presence of external magnetic fields are required to study the domain evolution and dynamics. Among the aforementioned methods, only MFM meets the requirements needed to obtain information on the magnetic structure in the sub-micrometer range, in the presence of an external field.

Multilayer films with alternating ferromagnetic layers, in particular multilayers containing ultrathin Co layers (typically 2–5 Å), can exhibit strong perpendicular anisotropy.^{13,14,16-23} The interest for these material combinations is at least partially triggered by the possibility to replace expensive rare earth alloys by Co-based materials in magneto-optical recording media. Here, we present results from investigations of the domain structure in an epitaxial bcc Fe₈₁Ni₁₉/Co (001) superlattice. We discuss the field dependence of the domain width and address the origin of the perpendicular anisotropy.

II. EXPERIMENT

Fe₈₁Ni₁₉/Co superlattices were grown on MgO(100) single crystal substrates, using dc magnetron sputtering from

separate Fe₈₁Ni₁₉ (purity 99.99 %) and Co (purity 99.95 %) targets arranged in a cluster geometry. The MgO(100) single-crystal substrates were introduced into the growth chamber and out-gassed at about 700 °C for 1 h under ultra-high-vacuum conditions before deposition. An optimal growth temperature of 170 °C for the superlattices was determined, by growth samples at temperatures between 100 °C and 400 °C. The background pressure was typically 1.5 · 10⁻⁹ Torr. During deposition, the argon (of 99.99 % purity) flow was controlled for obtaining a partial pressure of 2.5 · 10⁻³ Torr resulting in deposition rates of 0.035 nm/s and 0.08 nm/s for FeNi and Co, respectively. The deposition rates were obtained by calibrated *in situ* quartz microbalance. Finally, the actual thicknesses and the repeat distance were determined using x-ray reflectivity and diffraction. The thickness of the layers, in the sample discussed here, were 2.25 nm for the FeNi and 1.95 nm for the Co layers with 100 repetitions. Thus, the total thickness of the sample was 420 nm.

The crystallographic structure of the superlattice was investigated by high angle (2 Θ = 50°–80°) x-ray diffraction using Siemens D5000 diffractometer (Cu-K α), which confirmed good crystalline quality of the superlattice (not shown here). The full width at half maximum (FWHM) of the rocking curve of the (002) reflection was 0.3 °.

Magnetization measurements were performed, using the magneto-optical Kerr effect (MOKE) in the longitudinal configuration with s-polarized light. The experimental setup allows for the rotation of the sample around its surface normal, making measurements in arbitrary in-plane directions possible. More details of the experimental MOKE setup can be found in Ref. 24.

Figure 1 shows a typical in-plane (longitudinal geometry) MOKE magnetization loop of the Fe₈₁Ni₁₉/Co superlattice, measured at room temperature. The shape of the loop is typical for films with stripe domain structure.²⁸ The coercivity is approximately 8 mT and the remanent magnetization is around 0.6M_s (M_s is the saturation magnetization) showing that the magnetization vector is tilted approximately 50 ° out of the film plane.

No change of the magnetization was observed when ro-

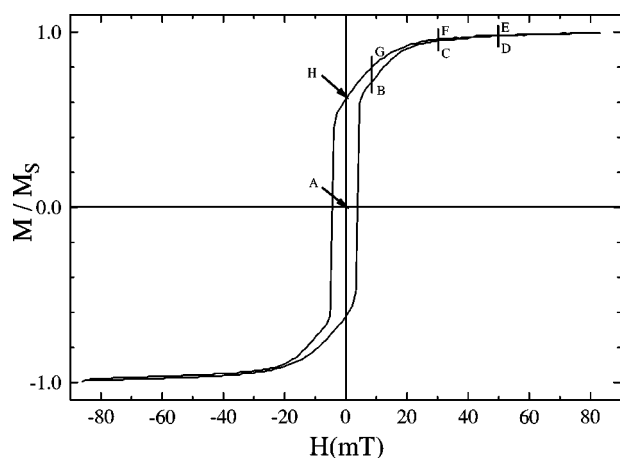


FIG. 1. The MOKE hysteresis loop of the 420 nm thick $\text{Fe}_{81}\text{Ni}_{19}/\text{Co}$ superlattice. The marks labeled on the curve correspond to the typical regimes of the magnetization process and corresponding MFM images are shown in Fig. 2.

tating the sample with respect to the field, i.e., the overall in-plane magnetic anisotropy is negligible as compared to the coercivity indicating a “conical anisotropy” depending on the direction of a previous saturation field.

The magnetization curve can be divided into two different regions: the low-field region from zero fields through the coercivity field, where a small increase of the applied field gives fast rise of the magnetization, and the high-field region from above the coercive field to the saturation field, where a large increase of the field induces only small changes on the in-plane magnetization.

The imaging of the magnetic domains was performed

with a magnetic force microscope (digital instruments, DI 3100) operated in tapping-lift mode. This mode allows simultaneous acquisition and clear separation between the spatial and the magnetic topography. A permanent magnet system was used to achieve a variable external magnetic field during imaging.²⁵ Such an applied field during MFM imaging affects both the probe and the sample.^{26,27} Therefore, the response of the probe to magnetic fields must be well known. Various types of commercially available tips with low (Fe-CoNi coating) and high (CoCr coating) coercivity were tested prior to the image acquisition. All the tips were magnetized vertically with a permanent magnet (along the needle). A set of measurements was performed on the same sample using different types of tips to verify the reproducibility and to exclude artifacts from remagnetization of the tips. The extracted domain periods were essentially the same. The MFM image contrast is proportional to the gradient of the magnetic force between tip and sample. In order to elucidate the tip influence on the domain structure, the tip-to-sample distance was varied in the range from 50 to 150 nm during magnetic imaging. The images were analyzed by applying a two-dimensional Fourier transform (2DFT) algorithm. The 2DFT analysis enabled determination of the average domain period, perpendicular to the average stripe direction, and the angular distributions of the stripes relative to the direction of the externally applied field.

MFM imaging was performed in the following way: initially an MFM measurement was done in the virgin state, in the absence of an external field. Thereafter a field of 8.3 mT was applied and a new MFM image was acquired. This procedure was repeated at the fields indicated in Fig. 1, with initially increasing and thereafter decreasing field. The re-

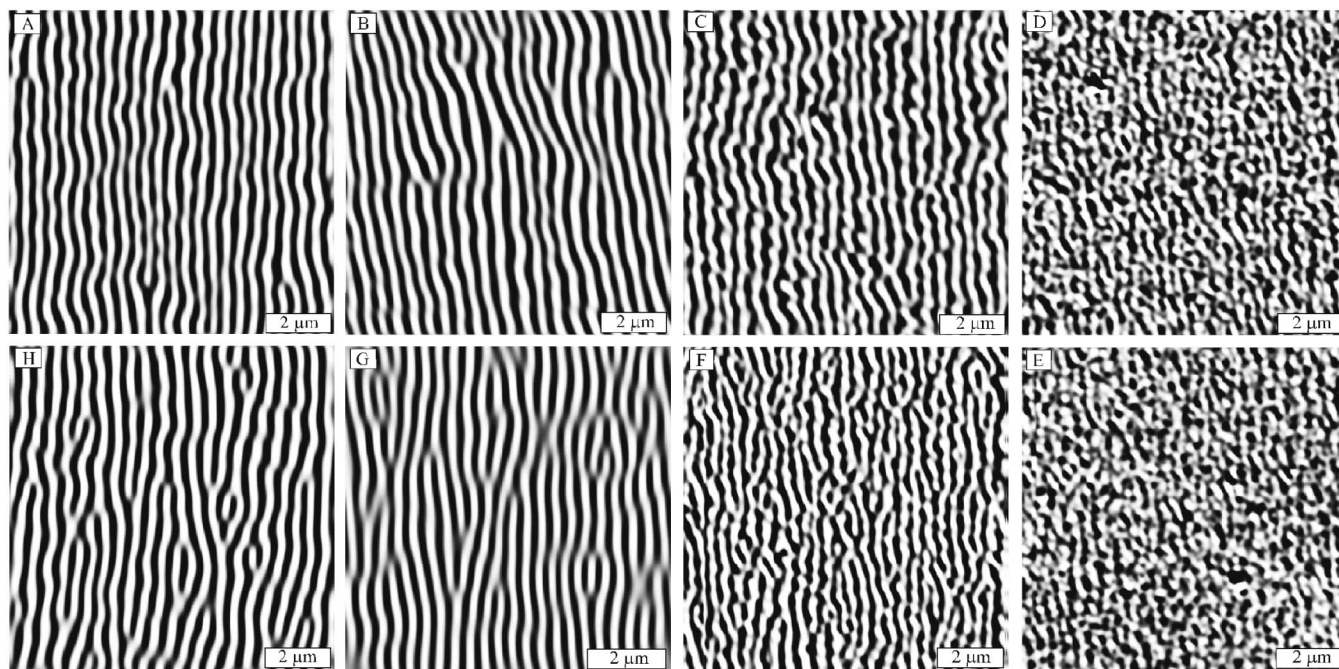


FIG. 2. The MFM images of the 420 nm thick $\text{Fe}_{81}\text{Ni}_{19}/\text{Co}$ superlattice at different externally applied in-plane magnetic fields: (a)—virgin (nonmagnetized) state; (b), (c), (d)—increasing field 8.3, 30, and 50 mT; (e), (f), (g)—decreasing field 50, 30, 8.3 mT; (h)—in remanent state.

sults are displayed in Fig. 2. The MFM imaging confirms the existence of out-of-plane magnetization in the sample, consistent with perpendicular magnetic anisotropy. The dark (light) regions indicate the direction of local magnetization direction in (out) of the film plane. The virgin domain structure [prior to applying a magnetic field, see Fig. 2(a)], consists of parallel stripe domains. Such stripe domain structures in ferromagnetic materials arise from a balance between the magnetocrystalline, dipolar, and exchange energies. Alternate domains have magnetization in opposite directions and therefore are separated by Bloch walls the widths of which are determined by a balance between magnetocrystalline and exchange energies.²⁸ Above a critical thickness, the perpendicular component of magnetization turns to align periodically up and down relative to the film surface (stripe domains), as was predicted by Kittel.²⁹ The film will favor formation of closure domains at the expense of the anisotropy energy. Only for the case of strong perpendicular anisotropy can the magnetization be regarded as completely aligned along the perpendicular direction. In the sample under consideration the domain structure will also be modified by the interaction between the layers. Here, the layers can be regarded as a single magnetic entity, due to the strong inter-layer coupling. The independent magnetic layers would give rise to domain structures with different sizes and different directions of the magnetization vector.

The influence of the external field on the domain structure was also studied. Corresponding MFM images are presented in Figs. 2(b)–2(h). The average domain period was observed to increase with increasing field, from the virgin (nonmagnetized) state through the coercive region. Above the coercive field, the average domain period decreases again and the image contrast decreases. The increment beyond the coercive field makes the stripes wavy and irregular in shape. At approximately 50 mT, these collapse and form irregular segments. The average domain periods become unmeasurable at fields about 60 mT. It is important to note that the sign of the perpendicular component did not reverse, while passing through the coercive field, i.e., the positions of the stripes measured at different applied fields are essentially the same. Thus, the direction of the perpendicular component is not affected. Thereafter the sample was saturated at 130 mT and the field decreased back to zero. When the field is reduced after saturation, a periodic stripe domain structure is formed again with the stripes aligned in the direction of the applied field showing a reversible magnetization process. The stripe domains become more regular with decreasing fields, but exhibit clear differences in the domain period as compared to the virgin state indicating about irreversible processes below the coercivity field. The dependence of the domain period on the field is shown in Fig. 3. As seen in the figure, the measured average domain period increases with decreasing field but does not go through a maximum, as in the initial magnetization process. Similar observations of stripe domain variations were found in Fe-based thin films^{16,30} and in multilayers¹² at high fields.

III. THEORY

A. Different magnetic contributions to the total energy

To explain the experimental results presented above we consider a model of a multilayer consisting of N bilayers.

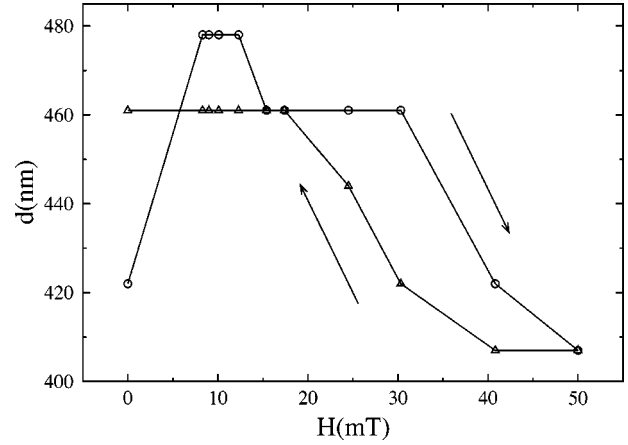


FIG. 3. The dependence of the average period of the stripe domains in the 420 nm thick $\text{Fe}_{81}\text{Ni}_{19}/\text{Co}$ superlattice on in-plane applied external magnetic field. The value of 420 nm at 0 mT corresponds to the virgin state [Fig. 2(a)].

Each bilayer consists of two ferromagnetic sublayers, labeled 1 and 2 with thicknesses t and s and $D = s + t$. The spontaneous magnetizations of the sublayers will be denoted by $M_s^{(1)}$ and $M_s^{(2)}$, respectively. The in-plane magnetization component is assumed to be completely aligned along the positive stripe axes y , which coincides with the direction of the applied field. This assumption should apply for the branch through the points E, F, G, and H of the hysteresis loop (Fig. 1), where the external field decreases. The perpendicular magnetization component is periodically aligned along $\pm z$ with the period $d = d_1 + d_2$, so that the magnetization direction points with an angle θ with respect to the surface normal. The situation is sketched in Fig. 4. The domains are thus separated by Bloch walls in which the magnetization rotates gradually from the angle θ to $\pi - \theta$, assuming symmetric walls. The wall plane between two domains is parallel to the yz plane. The domain walls are assumed to be at the same positions in all layers in order to minimize the magnetostatic energy. The total energy of this domain structure is the sum of four terms:

$$e = e_a + e_w + e_d + e_h, \quad (1)$$

where e_a is the anisotropy energy, e_w is the wall energy, e_d is the magnetostatic or demagnetizing energy, and e_h is the

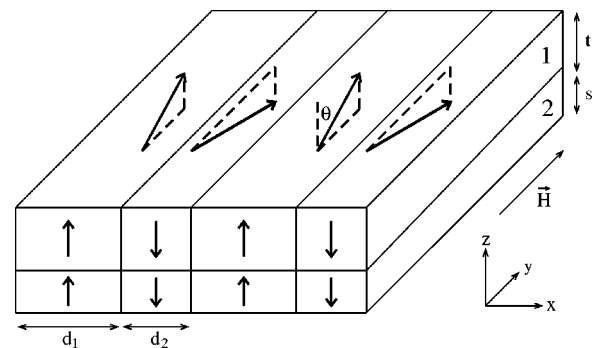


FIG. 4. Geometry and magnetization distribution as assumed for the calculation of the magnetization curves.

energy arising from the interaction of the magnetization with the applied field. Coercivity effects are neglected. All energies are calculated per unit volume and are normalized to the average demagnetizing energy constant $K_d = \mu_o/2[(M_s^{(1)})^2 t + (M_s^{(2)})^2 s]/D$. K_d corresponds to the stray field energy for a sample which is infinitely extended in the xy plane and uniformly magnetized perpendicular to its surface.

B. The anisotropy and wall energy

In the case of uniaxial anisotropy the corresponding energy can be expressed as

$$e_a = \beta_2 \sin^2 \theta + \beta_4 \sin^4 \theta + \dots, \quad (2)$$

where θ is the angle between the magnetization and the perpendicular axis and β_2, β_4 are the anisotropy constants. In the following we will only consider the first term in this expansion with $\beta_2 \equiv \beta$. For simplicity, we assume the anisotropy and exchange constants to be the same in both layers. For the case of the anisotropy it can be justified by an assumption that the latter is induced mainly by the interfaces; exchange parameters for Fe, Co, and Ni are the same only in the order of magnitude, so this simplification may not be very accurate quantitatively but seems to be adequate for qualitative analysis of the experimental data. However, using the same constants is further justified if the angle θ is approximately the same in both layers. In this case the constants play the role of effective constants for a bilayer. The wall energy will then correspond to the average over a bilayer and may be expressed as

$$e_w = \frac{2\tau}{d}, \quad (3)$$

where τ is the wall tension. In Appendix A we show that for the simple model of an one-dimensional wall it may be written as

$$\tau(\theta) = 4\tau_0[E(\cos \theta) - \sin^2(\theta)K(\cos \theta)] \quad (4)$$

with $\tau_0 = \sqrt{\alpha\beta}$, where α is an exchange parameter, $K(k)$ and $E(k)$ are the complete elliptic integrals of the first and second kind, respectively.³¹ The tension is plotted in Fig. 5. The total width of the domain wall is given by $2L$ with

$$L = \sqrt{\alpha/\beta}K(\cos \theta). \quad (5)$$

This expression does not vanish for $\theta = \pi/2$ as expected and diverges for $\theta = 0$, i.e., the 180° degree wall. The width of the wall should remain finite and vanish if the magnetization lies completely in plane. In order to obtain an expression with these properties, the length may be defined as the distance from the wall center on which the magnetization varies significantly, meaning that

$$\frac{d\tilde{\varphi}}{dx} \cong \tilde{\epsilon}, \quad (6)$$

where $\tilde{\epsilon}$ is a small positive parameter which has dimension of an inverse length. As shown in Appendix A, this requirement leads to

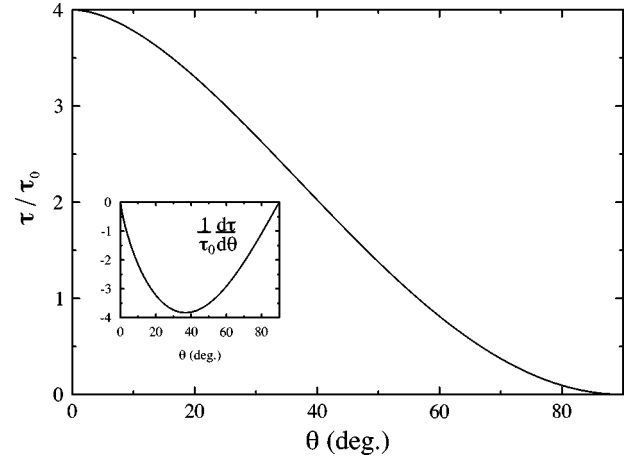


FIG. 5. Domain wall tension τ/τ_0 as a function of the angle θ . The inset shows the corresponding derivative.

$$\tilde{L} = L_0 F \left[\arcsin \left(\frac{\sqrt{\sin^2 \varphi - L_0^2 \tilde{\epsilon}^2}}{\sin \varphi} \right) \middle| \sin \varphi \right], \quad (7)$$

where $F(\phi|k)$ is the elliptic integral of the first kind, $\varphi = \pi/2 - \theta$ and $L_0 = \sqrt{\alpha/\beta}$. The domain wall width is plotted in Fig. 6 for several values of the dimensionless parameter $\epsilon = L_0 \tilde{\epsilon}$. Note that expression (5) is regained for $\epsilon = 0$.

C. The magnetostatic energy

The magnetostatic energy can be split into two contributions, one arising from the perpendicular component and the other from the in-plane component of the magnetization. The latter one is due to the finite extensions of the sample, i.e., the magnetic charges on the sample edges. This is a small term and it will for simplicity be included in the first term of the anisotropy energy expansion, Eq. (2), as a shape anisotropy, since it has the same angular dependence. A small z dependence is induced by the inhomogeneous field in the z direction and will be neglected here. For the calculation of

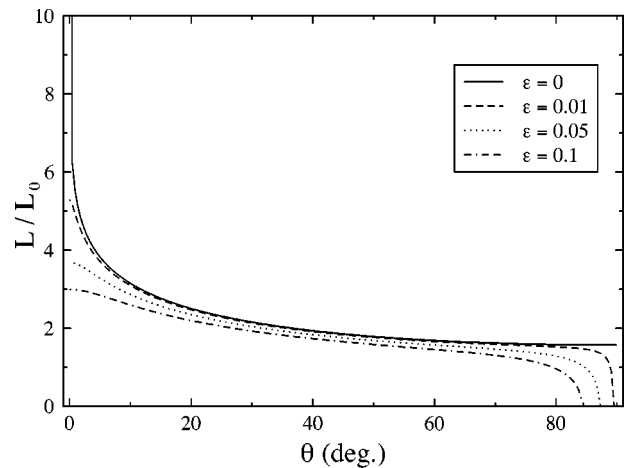


FIG. 6. Domain wall length L as a function of θ as given by Eq. (7) for different values of $\epsilon = L_0 \tilde{\epsilon}$. The case $\epsilon = 0$ coincides with definition Eq. (5). The total domain wall width is $2L$.

the demagnetizing energy arising from the perpendicular component, we assume a multilayer with infinite extensions in the xy plane and the magnetization being parallel everywhere along the z direction. In particular, we assume the interface exchange coupling between FeNi and Co strong enough so that the angle enclosed between the magnetization and the surface normal is the same for both types of layers. We further take the walls to be symmetric as required to minimize the wall energy. The z component of the magnetization in alternate domains thus is $M_z = \pm M_s \cos \theta$. The walls are assumed to be infinitely thin. For simplicity, we only give the expression for the symmetrical case $d_1 = d_2 = d/2$ here, since it may be proven that it does correspond to the minimal energy. A general expression for different d_1 and d_2 is given in Appendix B. The energy may then be written as

$$e_d = f(d) \cos^2 \theta, \quad (8)$$

where the d dependent part is

$$f(d) = \sum_{n \text{ odd}}^{\infty} \frac{4}{(n\pi)^3} \frac{d}{D} [w_1 f_n(t, d) + w_2 f_n(s, d) + w_3 g_n(d)], \quad (9)$$

with the following abbreviations

$$\begin{aligned} f_n(r, d) &= 1 - \exp\left(-2\pi n \frac{r}{d}\right) + \frac{\sinh^2\left(\pi n \frac{r}{d}\right)}{\sinh^2\left(\pi n \frac{D}{d}\right)} \\ &\times \left\{ \frac{1}{N} \left[1 - \exp\left(-2\pi n \frac{ND}{d}\right) \right] \right. \\ &\left. - \left[1 - \exp\left(-2\pi n \frac{D}{d}\right) \right] \right\}, \\ g_n(d) &= - \left[1 - \exp\left(-2\pi n \frac{t}{d}\right) \right] \left[1 - \exp\left(-2\pi n \frac{s}{d}\right) \right] \\ &+ 2 \frac{\cosh\left(\pi n \frac{D}{d}\right) \sinh\left(\pi n \frac{t}{d}\right) \sinh\left(\pi n \frac{s}{d}\right)}{\sinh\left(\pi n \frac{D}{d}\right) \sinh\left(\pi n \frac{D}{d}\right)} \\ &\times \left\{ \frac{1}{N} \left[1 - \exp\left(-2\pi n \frac{ND}{d}\right) \right] \right. \\ &\left. - \left[1 - \exp\left(-2\pi n \frac{D}{d}\right) \right] \right\} \end{aligned}$$

with $r = s, t$. The dimensionless factors w_i are defined by $w_i = [(M_s^{(i)})^2] D / [(M_s^{(1)})^2 t + (M_s^{(2)})^2 s]$, $i = 1, 2$, and $w_3 = (M_s^{(1)} M_s^{(2)}) D / [(M_s^{(1)})^2 t + (M_s^{(2)})^2 s]$. The first two terms in brackets in Eq. (9) correspond to the self-energies of the respective sublattices. The third term stems from their interaction and is a negative one.

D. The external field

Finally, the interaction of the magnetization with the applied field contributes a term

$$e_h = \frac{-\mu_0 H M_s \sin \theta}{K_d} = -2hm \sin \theta, \quad (10)$$

where $h = H / \sqrt{[(M_s^{(1)})^2 t + (M_s^{(2)})^2 s] / D}$ is the normalized field applied in the direction of the stripes and $m = M_s / \sqrt{[(M_s^{(1)})^2 t + (M_s^{(2)})^2 s] / D}$. The spontaneous magnetization of the sample is the average of the spontaneous magnetizations of the sublayers: $M_s = (M_s^{(1)} t + M_s^{(2)} s) / D$.

We now minimize the total energy with respect to the parameters d and θ , i.e., $\partial e / \partial d = 0$, $\partial e / \partial \theta = 0$. This yields

$$d = \frac{1}{\cos \theta} \left[2\tau(\theta) / \left(\frac{\partial f(d)}{\partial d} \right) \right]^{1/2}, \quad (11)$$

$$h = \frac{1}{m} \left[[\beta - f(d)] \sin \theta + \frac{1}{d \cos \theta} \frac{\partial \tau}{\partial \theta} \right]. \quad (12)$$

As is seen from Eq. (12), the magnetostatic- and wall energy tend to decrease the field ($\partial \tau / \partial \theta < 0$), i.e., force the magnetization into plane, whereas the anisotropy tends to increase it. The calculation procedure is to choose an angle θ and a corresponding magnetization $M_{\parallel} = M_s \sin \theta$ parallel to the film surface, calculate d from the implicit Eq. (11) and obtain the corresponding field from Eq. (12). The exchange and anisotropy constants are used as fitting parameters to yield a zero applied field h where the in-plane magnetization equals the remanence $M = M_r$, and d equals the domain period d_r in the remanent state. They are uniquely determined by this condition. For the calculation presented below we take $M_r / M_s = 0.6$ and $d_r = 460$ nm.

We further assume bcc structure with lattice constants and spontaneous magnetizations $a = 0.282$ nm and $M_s = 1.73 \mu_B / \text{Atom}$ for the Co-layers and $a = 0.286$ nm and $M_s = 2.25 \mu_B / \text{Atom}$ for the FeNi-layers.

IV. THEORETICAL RESULTS AND DISCUSSION

The fitting procedure correspondingly leads to the values $K_u = \beta K_d = 5.38 \times 10^5 \text{ J/m}^3$ and $A = \alpha K_d = 4.66 \times 10^{-10} \text{ J/m}^2$, for the anisotropy and exchange constants. For these parameters, the magnetization and domain period as functions of the applied field are shown in Figs. 7 and 8, respectively. We find qualitative agreement with the experimental results: the domain period decreases with increasing applied field, although somewhat too slowly compared to the experiment. Also, the saturation field at which $M_{\parallel} / M_s = 0.99$ is too high, with some 40% deviation.

The ratio of the domain wall width ($2L_0 \approx 60$ nm) to the stripe period is not too small which indicates a discrepancy between theory and experiment already for zero applied field. We would also expect a smaller exchange constant. For

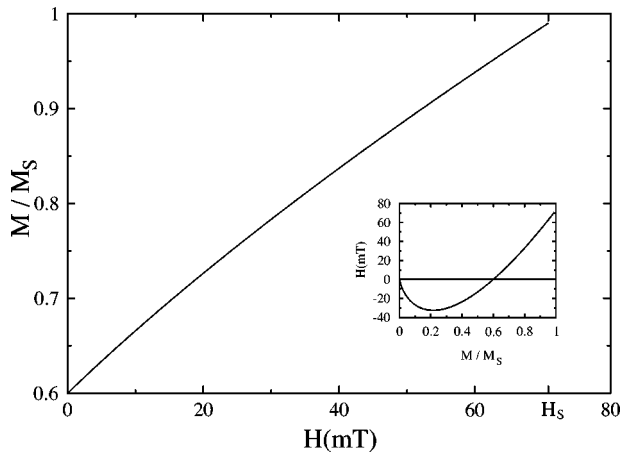


FIG. 7. Magnetization curve as calculated from Eqs. (11) and (12). The saturation field is approximately 70 mT. The inset shows the applied field needed to obtain a certain in-plane magnetization under the assumption that the in-plane component remains aligned along the positive y axis.

the quality factor Q , which is defined as the ratio between the anisotropy and the demagnetizing energy constant, $Q = K_u/K_d$, we have $Q = \beta = 0.32$. It is known that such a Q value may lead, for a single layer, to the formation of closure domains.²⁸ Formation of partial flux closure domains on the sample surface, which would also be consistent with the MFM images, yields a smaller magnetostatic energy as the one calculated here and leads to erroneous estimates of the exchange and anisotropy constants, thus affecting the entire calculation. In particular, a smaller value of the $f(d)$ term would lead to a smaller anisotropy constant and consequently to a smaller saturation field.

A principal difficulty is to calculate the dependence of the wall energy on the wall angle and in particular in an applied field, since the wall structure of the superlattice is not known. Deviations are expected because the proposed domain wall model is not strictly applicable to these films, since the walls may have a two-dimensional structure. The

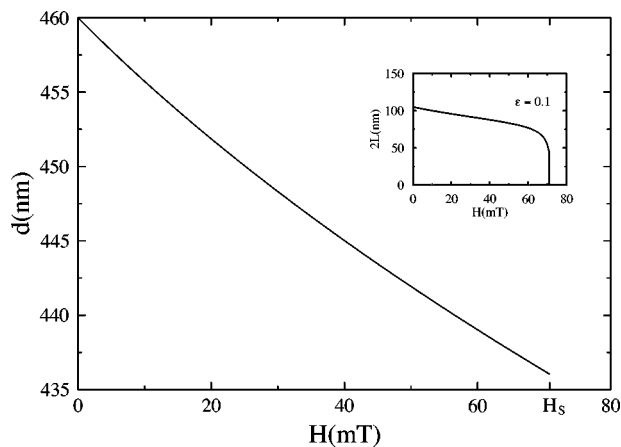


FIG. 8. Domain period d as a function of the applied field. The period decreases down to approximately 435 nm at saturation. The inset shows the dependence of the wall width $2L$ on the applied field, where L is given by Eq. (7) for $\epsilon = 0.1$.

problem becomes even more complicated, if closure domains have to be taken into account. Deviations for high fields are due to the effect of the external field on the wall tension which has not been taken into account. In an applied field, the wall tension is expected to decrease faster than according to Eq. (4), allowing for smaller domain periods at high fields.

Furthermore, the proposed stripe distribution of the magnetization does not correspond to the real structure at high magnetic fields. The collapse of the stripes at high fields (Fig. 2) will change (lower) the demagnetizing energy. Also, the wall energy increases because of additional walls in the system (below we will discuss this point in more detail). These effects are not accounted for in the present model but are presumably small because the energies of the two domain structures are expected to be quite close.

Although the model is too simple to allow for quantitative predictions, it shows that the competition between the anisotropy energy favoring perpendicular magnetization and the demagnetizing and wall energy favoring in-plane magnetization stabilizes the magnetization at an oblique angle with respect to the film surface, giving rise to an “effective” easy axis. The tilt angle depends on the exchange and anisotropy constants. The easy axis can be rotated by simply rotating the in-plane magnetization component in an applied field, resulting in the observed rotatable anisotropy.

The observed domain structure, however, requires a sizable perpendicular anisotropy. It was reported by Draaisma, den Broeder and de Jonge³² for Co/Pd multilayers that the preferred magnetization direction became perpendicular to the film plane for Co thicknesses below about 0.8 nm. Perpendicular magnetization was also found for Co-layer thicknesses below 1.4 nm in Co/Au multilayers induced by interface sharpening after annealing.³³ In our case we find perpendicular anisotropy for 1.95 nm thick Co layers, consistent with sharp interfaces between FeNi and Co.

To gain further insight in the collapse of the stripes, we calculated the magnetostatic energy in a similar fashion as done in the appendix, but for the simpler case of a multilayer consisting of alternating magnetic and nonmagnetic layers. The somewhat lengthy expression is not shown here. The magnetization is now allowed to be also periodic along the stripe direction with period p , leading to a chesslike magnetization pattern for equal periods $d = p$. The demagnetizing energy for this pattern was confirmed to be smaller than for the stripe domains with the same period. However, the energies of the two structures are quite close as the energy of the checker is only about 5% smaller. The energy was minimized with respect to the unknowns θ , d , and p . If the tension of the additional Néel walls was taken to be larger than the tension of the Bloch walls separating the stripe domains, $\tau_N > \tau_B$, the period p tended to infinity, leading to a stripe domain structure. The reason is that although the demagnetizing energy decreases with decreasing p , the total energy increases, since the wall energy increases more strongly, unless τ_N is very small. Artificially taking the same wall energy term Eq. (3) for the Néel walls to regain symmetry leads to $d = p$. The model is too simple to describe the observed transition, but it is consistent with the following qualitative explanation of the collapse of the stripes:

The magnetostatic interaction favors formation of small domains. The demagnetizing energy term is thus smaller for the segment structure shown in Figs. 2(d) and 2(e) than for the stripe domain structure. However, the formation of smaller segments requires formation of additional walls along the stripe direction. These walls are Néel walls and are therefore expected to have a larger energy than the Bloch walls separating the stripe domains. Thus, formation of additional walls in this direction is unfavorable, so that stripe domains are preferred. For large angles θ and high fields, however, the difference between the wall energies for the two types of walls decreases as they approach zero. The situation then becomes approximately symmetric, leading to the collapse of the stripes. This is consistent with the MFM images (Fig. 2). It is indeed difficult to identify the original stripe direction after the collapse of the stripes. A larger wall energy for the Néel walls along the stripe direction also explains that the stripe direction is always found to coincide with the direction of the in-plane magnetization component.

More quantitatively, an instability of the stripe domain structure has been explained in Ref. 34 in terms of a simple Ising-like model with the z component of the magnetization, $m(\mathbf{r})$, which is uniform in the z -direction (normal to the film plane), so $\mathbf{r}=(x,y)$. The magnetostatic energy of the film of thickness D can be written as the energy of a plane capacitor with magnetic charges $\pm m(\mathbf{r})$ so that

$$E_m = \int \int d\mathbf{r} d\mathbf{r}' m(\mathbf{r}) m(\mathbf{r}') \left[\frac{1}{|\mathbf{r}-\mathbf{r}'|} - \frac{1}{\sqrt{(\mathbf{r}-\mathbf{r}')^2 + D^2}} \right] \\ = 2\pi \sum_{\mathbf{q}} m_{\mathbf{q}} m_{-\mathbf{q}} \frac{1 - e^{-qD}}{q}, \quad (13)$$

where $m_{\mathbf{q}}$ is a two-dimensional Fourier component of the magnetization density. At the same time, the exchange energy can be written as

$$E_{exch} = \frac{1}{2} \alpha \sum_{\mathbf{q}} q^2 m_{\mathbf{q}} m_{-\mathbf{q}}, \quad (14)$$

so there is a finite value of the wave vector $q=q^*$ found from the condition

$$\frac{d}{dq} \left(2\pi \frac{1 - e^{-qD}}{q} + \frac{1}{2} \alpha q^2 \right) = 0 \quad (15)$$

with a minimal energy of the magnetic fluctuations and the system may be unstable with respect to the corresponding modulation. This instability may also be described in terms of the production of linear defects (disclinations) which can be clearly seen in Fig. 2.^{35,36} It is interesting to note that the development of the instability is similar in some sense to a formation of a “stripe glass state” in Ginzburg-Landau systems with long-range Coulomb interaction and the global constraint that the average order parameter is equal to zero.³⁷ In both cases it is important that the condition [Eq. (15)] (or equivalent one for the Coulomb interaction) determines only the length of the wave vector for optimal fluctuations but not its directions, which leads to a strongly frustrated situation. Coming back to the real experimental situation one should

remember that the “Ginzburg-Landau” case corresponds to strong magnetic fields when the perpendicular component of the magnetization is sufficiently small. The formation of quasichaotic patterns for the multilayers under consideration will be considered in more details elsewhere.

The hysteretic d dependence is directly connected to the different magnetization structures in the two branches of the hysteresis curve. In the branch through the points B, C, and D, the in-plane magnetization is not completely aligned along the positive stripe axis. This leads to different values of the competing energy terms in Eq. (1), so that the domain period consequently gets shifted. The low d value in the virgin state and its sudden increase when applying an external field could be explained by a domain structure in which the easy-axis domains are separated by 180 degree Bloch walls. The competition between the corresponding wall energy and the other energy terms determines the observed d value. Under an external field applied in the y direction, the magnetization will flip from the perpendicular direction into the effective easy-axis direction (as determined by the competition between the energy terms), giving rise to a different domain period.

It is instructive to calculate the magnetization at in-plane magnetization values smaller than the remanence. The result is shown in the inset of the Fig. 7. Under the assumption that the magnetization remains aligned along the positive y axis, a strong field larger than the coercive field in the opposite direction would be needed to turn the magnetization around in this way. If such a field is applied, large changes in the field will only cause small changes in the magnetization, until the coercive field is reached and switching occurs.

Temperature effects may be ignored in our phenomenological approach since we take the observed domain structure as given for the calculation of the energy terms. The magnetization direction \mathbf{M} is thereby understood as the average over the fluctuations. Quantitatively convincing results have been obtained using a similar method for determining equilibrium values of the variational parameters.³⁸

In particular cases the energy minima can be very shallow, suggesting that at finite temperatures a finite range of equilibrium values would be allowed.³⁹ For the domain period this might lead to somewhat more irregular structures. In our case the minima appeared to be well defined.

Nevertheless, the observed domain structure is expected to exhibit a temperature dependence which in our model enters via the exchange and anisotropy constants, which are known to be temperature dependent. In the present study, we only consider the domain structures at room temperature.

V. CONCLUSIONS

Dense stripe domains were observed in a $\text{Fe}_{81}\text{Ni}_{19}/\text{Co}$ superlattice grown on $\text{MgO}(100)$ single-crystal substrates, using dc magnetron sputtering. This type of domain structure arises due to the existence of out-of-plane anisotropy in the film, which is argued to originate from interface induced anisotropy. The energy of the domain wall is dominant in the magnetization process, which was found to be reversible above the coercivity field. In addition, the stripe period

showed strong and hysteretic dependence on the applied field, as observed by MFM imaging. A phenomenological model has been put forward that correctly predicts a decreasing domain period with increased applied field. The discrepancy between theory and experiment can be attributed to the formation of partial flux closure domains on the sample surface.

ACKNOWLEDGMENTS

Financial support from the Swedish Research Council (VR), the Swedish Foundation for Strategic Research (SSF), and Göran Gustafsson Foundation are acknowledged.

APPENDIX A: DOMAIN WALL

The exchange and anisotropy energies are given by

$$E_{ex} = \frac{\mu_0}{2} M^2 \alpha (\tilde{\theta}'(x))^2, \quad E_a = \frac{\mu_0}{2} M^2 \beta \sin^2 \tilde{\theta}(x), \quad (\text{A1})$$

where the prime denotes differentiation with respect to x . For the calculation it is convenient to transform to the angle $\varphi = \pi/2 - \theta$, which better reveals the symmetry. Note that in order to distinguish the angles in the walls, which are functions of the coordinate x , from the angles in the domains (θ , φ), they will be marked by a tilde: $\tilde{\varphi}(x)$, $\tilde{\theta}(x)$. The wall tension $\tau = \sigma_w / \mu_0 / 2M^2$ is the integral

$$\tau = \int_{-L}^L [\alpha (\tilde{\varphi}'(x))^2 + \beta \cos^2 \tilde{\varphi}(x)] dx. \quad (\text{A2})$$

The function that minimizes the tension is a solution to the corresponding Euler equation $\alpha \tilde{\varphi}''(x) = -\beta \sin \tilde{\varphi} \cos \tilde{\varphi}$ with boundary conditions

$$\tilde{\varphi}(\pm L) = \pm \varphi, \quad \tilde{\varphi}'(x)|_{\pm L} = 0. \quad (\text{A3})$$

The requirement for the tension to be a solution to the Euler equation leads to a symmetric wall. A first integral that satisfies these boundary conditions is $[\tilde{\varphi}'(x)]^2 = (\beta/\alpha)[\sin^2 \varphi - \sin^2 \tilde{\varphi}(x)]$. This may be used to rewrite the tension, Eq. (A2), as

$$\tau = 2\beta L (\sin^2 \varphi + 1) - 2\beta \int_{-L}^L \sin^2 \tilde{\varphi}(x) dx. \quad (\text{A4})$$

The remaining integral can be evaluated replacing dx by $d\tilde{\varphi} / \sqrt{(\beta/\alpha)(\sin^2 \varphi - \sin^2 \tilde{\varphi})}$ and using the substitution $\tilde{\varphi}(\psi) = \arcsin(\sin \varphi \sin \psi)$, which transforms the occurring integrals to standard complete elliptic integrals. Inserting the result into Eq. (A4), replacing the width $2L$ given by

$$2L = 2 \sqrt{\frac{\alpha}{\beta}} \int_0^\varphi \frac{d\tilde{\varphi}}{\sqrt{\sin^2 \varphi - \sin^2 \tilde{\varphi}}} = 2 \sqrt{\frac{\alpha}{\beta}} K(\sin \varphi), \quad (\text{A5})$$

and transforming back to the angle θ yields

$$\tau = 2 \sqrt{\alpha \beta} ((\cos^2 \theta - 1)K(\cos \theta) + 2E(\cos \theta)). \quad (\text{A6})$$

This expression, however, does not vanish for $\theta = \pi/2$ as expected. To resolve the problem, consider the sum of the anisotropy and wall energy:

$$e_w + e_a = \frac{2\tau}{d} + \frac{(d-4L)}{d} \beta \sin^2 \theta, \quad (\text{A7})$$

which obviously holds for $4L < d$. In the case $4L > d$ the walls may be cut off at $L_c = d/4$, neglecting the exchange energy for large distances. Subtracting the additional anisotropy contribution $[(4L-d)/d]e_a$ eventually leads to the same expression as Eq. (A7). Redefining the tension as $\tau \rightarrow \tau - 2L\beta \sin^2 \theta$ leads to the expression given in the text.

In order to obtain Eq. (7) for the wall width, note that the condition $d\tilde{\varphi}/dx|_{x=\tilde{L}} = \tilde{\epsilon}$ uniquely determines \tilde{L} since $d\tilde{\varphi}/dx$ is a strictly monotonic decreasing function. Using the first integral it can be rewritten as $L_0^{-1} \sqrt{\sin^2 \varphi - \sin^2 \tilde{\varphi}(\tilde{L})} = \tilde{\epsilon}$, where $L_0 = \sqrt{\alpha/\beta}$. Solving for $\tilde{\varphi}$ gives

$$\tilde{\varphi}(\tilde{L}) = \arcsin(\sqrt{\sin^2 \varphi - L_0^2 \tilde{\epsilon}^2}). \quad (\text{A8})$$

The function $x(\tilde{\varphi})$ is easily obtained by taking the first integral, separating variables and integrating, giving $x(\tilde{\varphi}) = L_0 F(\arcsin(\sin \tilde{\varphi} / \sin \varphi) | \sin \varphi)$. Equating the expression for the inverse $\tilde{\varphi}(x) = \arcsin(\sin \varphi \sin(F^{-1}(x/L_0) | \sin \varphi))$ for $x = \tilde{L}$ with Eq. (A8) and solving for \tilde{L} gives the desired result.

APPENDIX B: DEMAGNETIZING ENERGY

The expression for the demagnetizing energy of a multilayer consisting of alternating ferromagnetic and non-magnetic layers was already obtained by Draaisma and de Jonge.⁴⁰ We extend the result to the case of bilayers consisting of two different ferromagnetic materials. Although the derivation of the potential for a single layer is very similar to their derivation, we will give a survey over the entire calculation for clarity.

The z component of the magnetization for a single ferromagnetic layer with spontaneous magnetization $M_s^{(1)}$ and the assumed geometry can be written as

$$M_z^{(1)}(x, z) = M_s^{(1)} \cos \theta_1, \quad -\frac{1}{2}d_1 \leq x < \frac{1}{2}d_1, \\ -M_s^{(1)} \cos \theta_2, \quad \frac{1}{2}d_1 \leq x < \frac{1}{2}d_1 + d_2, \quad (\text{B1})$$

if $-\frac{1}{2}t \leq z < \frac{1}{2}t$ and 0 otherwise. The magnetization is periodic in x with period d . The Fourier series expansion is

$$M_z^{(1)}(x, z) = \tilde{M}^{(1)} + \sum_{n=1}^{\infty} \frac{2M_s^{(1)}(\cos \theta_1 + \cos \theta_2)}{n\pi} \times \sin\left(\pi n \frac{d_1}{d}\right) \cos\left(2\pi n \frac{x}{d}\right), \quad (\text{B2})$$

where $\tilde{M}^{(1)} = M_s^{(1)}(\cos \theta_1 d_1/d - \cos \theta_2 d_2/d)$. In order to obtain the corresponding expression for the type 2 layers, the replacement $M_s^{(1)} \rightarrow M_s^{(2)}$ has to be made. To allow for different angles, θ_i is replaced by φ_i for $i=1,2$. The potential $\phi(x, z)$ is a solution to the Laplace equation $\nabla^2 \phi = 0$ with boundary conditions

$$\phi_o\left(x, \frac{1}{2}t\right) = \phi_i\left(x, \frac{1}{2}t\right), \\ -\frac{\partial \phi_o}{\partial z}\left(x, \frac{1}{2}t\right) = -\frac{\partial \phi_i}{\partial z}\left(x, \frac{1}{2}t\right) + M_z\left(x, \frac{1}{2}t\right). \quad (\text{B3})$$

ϕ_i denotes the potential inside the layer ($|z| < \frac{1}{2}t$) and ϕ_o outside the layer ($z > \frac{1}{2}t$). For $z < \frac{1}{2}t$, one has $\phi(x, z) = -\phi_o(x, -z)$ by antisymmetry. The solution for the type 1 layers is

$$\phi_o^{(1)} = \frac{1}{2}\tilde{M}^{(1)}t + \sum_{k=1}^{\infty} \frac{M_s^{(1)}d(\cos \theta_1 + \cos \theta_2)}{k^2\pi^2} \sin\left(\pi k \frac{d_1}{d}\right) \times \sinh\left(\pi k \frac{t}{d}\right) \cos\left(2\pi k \frac{x}{d}\right) \exp\left(-2\pi k \frac{z}{d}\right), \quad (\text{B4})$$

$$\phi_i^{(1)} = \tilde{M}^{(1)}z + \sum_{k=1}^{\infty} \frac{M_s^{(1)}d(\cos \theta_1 + \cos \theta_2)}{k^2\pi^2} \sin\left(\pi k \frac{d_1}{d}\right) \times \exp\left(-\pi k \frac{t}{d}\right) \cos\left(2\pi k \frac{x}{d}\right) \sinh\left(2\pi k \frac{z}{d}\right). \quad (\text{B5})$$

To obtain the solution for the layers of type 2 the same replacements as made in the corresponding expression for the magnetization apply; additionally, t has to be replaced by s . The potential generated by sublattice 1 in bilayer p is found by proper superposition. Placing the bilayer with the center of the type 1 sublayer at $z=0$ and the center of the type 2 sublayer at $z = -\frac{1}{2}(s+t)$, the potential is [$\phi_p^{(1)}(x, 0) = 0$]:

$$\phi_p^{(1)}(x, z) = \sum_{j=1}^{p-1} \{\phi_o^{(1)}(x, z + (p-j)D) - \phi_o^{(1)}(x, (p-j)D)\} \\ - \sum_{j=p+1}^N \{\phi_o^{(1)}(x, (j-p)D - z) \\ - \phi_o^{(1)}(x, (j-p)D)\} \\ + \begin{cases} \phi_i^{(1)}(x, z) & , -\frac{1}{2}t \leq z < \frac{1}{2}t \\ -\phi_o^{(1)}(x, -z) & , -\frac{1}{2}t - s \leq z < -\frac{1}{2}t. \end{cases} \quad (\text{B6})$$

The corresponding potential generated by sublattice 2 in bilayer p is [$\phi_p^{(2)}(x, 0) = 0$]:

$$\phi_p^{(2)}(x, z) = \sum_{j=1}^{p-1} \{\phi_o^{(2)}(x, z + (p-j)D + \frac{1}{2}(s+t)) - \phi_o^{(2)}(x, (p-j)D + \frac{1}{2}(s+t))\} - \sum_{j=p+1}^N \{\phi_o^{(2)}(x, (j-p)D - z - \frac{1}{2}(s+t)) \\ - \phi_o^{(2)}(x, (j-p)D - \frac{1}{2}(s+t))\} + \begin{cases} \phi_i^{(2)}(x, z + \frac{1}{2}D) - \phi_o^{(2)}(x, \frac{1}{2}D), & -\frac{1}{2}t - s \leq z < -\frac{1}{2}t \\ \phi_o^{(2)}(x, z + \frac{1}{2}D) - \phi_o^{(2)}(x, \frac{1}{2}D), & -\frac{1}{2}t \leq z < \frac{1}{2}t. \end{cases} \quad (\text{B7})$$

The total potential generated in bilayer p is $\phi_p(x, z) = \phi_p^{(1)}(x, z) + \phi_p^{(2)}(x, z)$. The demagnetizing energy for layer p can be written as

$$E_p = \frac{\mu_0}{2dD} \int_0^d dx \{M_z^{(1)}(x, \frac{1}{2}t) [\phi_p(x, \frac{1}{2}t) - \phi_p(x, -\frac{1}{2}t)] \\ + M_z^{(2)}(x, -\frac{1}{2}t) [\phi_p(x, -\frac{1}{2}t) - \phi_p(x, -\frac{1}{2}t - s)]\}. \quad (\text{B8})$$

The term in brackets can further be rearranged into the following three contributions:

$$M_z^{(1)}(x, \frac{1}{2}t) [\phi_p^{(1)}(x, \frac{1}{2}t) - \phi_p^{(1)}(x, -\frac{1}{2}t)] \\ + M_z^{(2)}(x, -\frac{1}{2}t) [\phi_p^{(2)}(x, -\frac{1}{2}t) - \phi_p^{(2)}(x, -\frac{1}{2}t - s)] \\ + [M_z^{(1)}(x, \frac{1}{2}t) [\phi_p^{(2)}(x, \frac{1}{2}t) - \phi_p^{(2)}(x, -\frac{1}{2}t)] \\ + M_z^{(2)}(x, -\frac{1}{2}t) [\phi_p^{(1)}(x, -\frac{1}{2}t) - \phi_p^{(1)}(x, -\frac{1}{2}t - s)]]. \quad (\text{B9})$$

Inserting the expressions for M_z and ϕ_p into Eq. (B8) and carrying out the integration, only terms with $n=k$ remain. Averaging the result over all layers,

$$E_d = \frac{1}{N} \sum_{p=1}^N E_p, \quad (\text{B10})$$

the complete expression for the demagnetizing energy with the three contributions ordered according to Eq. (B9) can be written as follows:

$$\begin{aligned}
 E_d = \frac{\mu_0}{2} & \left[\left\{ M_s^{(1)} \left(\cos \theta_1 \frac{d_1}{d} - \cos \theta_2 \frac{d_2}{d} \right) \right\}^2 \frac{t}{D} + \sum_{n=1}^{\infty} \frac{(M_s^{(1)})^2 (\cos \theta_1 + \cos \theta_2)^2}{(n\pi)^3} \frac{d}{D} \sin^2 \left(\pi n \frac{d_1}{d} \right) f_n(t, d) \right. \\
 & + \left\{ M_s^{(2)} \left(\cos \varphi_1 \frac{d_1}{d} - \cos \varphi_2 \frac{d_2}{d} \right) \right\}^2 \frac{s}{D} + \sum_{n=1}^{\infty} \frac{(M_s^{(2)})^2 (\cos \varphi_1 + \cos \varphi_2)^2}{(n\pi)^3} \frac{d}{D} \sin^2 \left(\pi n \frac{d_1}{d} \right) f_n(s, d) \\
 & \left. + \sum_{n=1}^{\infty} \frac{M_s^{(1)} M_s^{(2)} (\cos \theta_1 + \cos \theta_2) (\cos \varphi_1 + \cos \varphi_2)}{(n\pi)^3} \frac{d}{D} \sin^2 \left(\pi n \frac{d_1}{d} \right) \times g_n(d) \right]. \quad (\text{B11})
 \end{aligned}$$

The explicit expressions for the terms $f_n(t, d)$, $f_n(s, d)$, and $g_n(d)$ are given in the text. The first two lines stem from the potential of one sublattice integrated over the *same* sublattice. Therefore, they correspond to the (averaged) self-energy of the respective sublattices. The third line stems from their interaction. Taking $d_1 = d_2 = d/2$ and $\theta_1 = \theta_2 = \varphi_1 = \varphi_2 = \theta$ and normalizing to the maximum magnetostatic energy, finally results in the expression given in the text.

-
- ¹P.F. Carcia, A.D. Meinhardt, and A. Suna, *Appl. Phys. Lett.* **47**, 178 (1985).
²P.F. Carcia, *J. Appl. Phys.* **63**, 5066 (1988).
³A.K. Menon and B.K. Gupta, *Nanostruct. Mater.* **11**, 965 (1999).
⁴S.-C. Shin, J.-H. Kim, and D.-H. Ahn, *J. Appl. Phys.* **69**, 5664 (1991).
⁵G. Bochi, H.J. Hug, D.I. Paul, B. Stiefel, A. Moser, I. Parashikov, H.J. Guntherodt, and R.C. O'Handley, *Phys. Rev. Lett.* **75**, 1839 (1995).
⁶R. Ploessl, J.N. Chapman, A.M. Tompson, J. Zweck, and H. Hoffmann, *J. Appl. Phys.* **73**, 2447 (1993).
⁷A. Tonomura, T. Matsuda, H. Tanabe, N. Osakabe, J. Endo, A. Fukuhara, K. Shinagawa, and H. Fujiwara, *Phys. Rev. B* **25**, 6799 (1982).
⁸M.R. Scheinfein, J. Unguris, J.L. Blue, K.J. Coakley, D.T. Pierce, P.J. Pyan, and R.J. Celotta, *Phys. Rev. B* **43**, 3395 (1991).
⁹R. Schäfer, B.E. Argyle, and P.L. Trouilloud, *IEEE Trans. Magn.* **28**, 2644 (1992).
¹⁰Th. Eimüller, R. Kalchgruber, P. Fischer, G. Schütz, P. Guttmann, G. Schmahl, M. Köhler, K. Prügl, M. Scholz, F. Bammes, and G. Bayreuther, *J. Appl. Phys.* **87**, 6478 (2000).
¹¹P. Castrucci, R. Gunnella, R. Bernardini, P. Falcioni, and M. De Crescenzi, *Phys. Rev. B* **65**, 235435 (2002).
¹²A. Asenjo, D. Garcia, J.M. Garcia, C. Prados, and M. Vazquez, *Phys. Rev. B* **62**, 6538 (2000).
¹³S. Hamada, K. Himi, T. Okuno, and K. Takanashi, *J. Magn. Magn. Mater.* **240**, 539 (2002).
¹⁴G. Ausanio, V. Iannotti, L. Lanotte, M. Carbuicchio, and M. Rateo, *J. Magn. Magn. Mater.* **226-230**, 1740 (2002).
¹⁵A. Asenjo, J.M. Garcia, D. Garcia, A. Hernando, M. Vazquez, P.A. Caro, D. Revelosona, A. Cebollada, and F. Briones, *J. Magn. Magn. Mater.* **196-197**, 23 (1999).
¹⁶S. Foss, C. Merton, R. Proksch, G. Skidmore, J. Schmidt, E.D. Dahlberg, T. Pokhil, and Y.-J. Cheng, *J. Magn. Magn. Mater.* **190**, 60 (1998).
¹⁷W.B. Zeper, F.J.A.M. Greidanus, P.F. Carcia, and C.R. Fincher, *J. Appl. Phys.* **65**, 4971 (1989).
¹⁸L. Louail, K. Ounadjela, M. Hehn, K. Khodjaoui, M. Gester, H. Danan, and R.L. Stamps, *J. Magn. Magn. Mater.* **165**, 387 (1997).
¹⁹R. Allenspach, M. Stampanoni, and A. Bischof, *Phys. Rev. Lett.* **65**, 3344 (1990).
²⁰S. Hamada, N. Hosoito, T. Ono, and T. Shinjo, *J. Magn. Magn. Mater.* **198-199**, 496 (1999).
²¹J.R. Barnes, S.J. O'Shea, M.E. Welland, J.-Y. Kim, J.E. Evetts, and R.E. Somekh, *J. Appl. Phys.* **76**, 2974 (1994).
²²L. Belliard, J. Miltat, V. Kottler, V. Mathet, C. Chappert, and T. Valet, *J. Appl. Phys.* **81**, 5315 (1997).
²³M. Speckmann, H.P. Oepen, and H. Ibach, *Phys. Rev. Lett.* **75**, 2035 (1995).
²⁴Z.Q. Qiu and S.D. Bader, *Rev. Sci. Instrum.* **71**, 1243 (2000).
²⁵R. Proksch, E. Runge, S. Fossi, B. Walsh, and P.K. Hansma, *J. Appl. Phys.* **78**, 3303 (1995).
²⁶K.L. Babcock, V.B. Elings, J. Shi, D.D. Awschalom, and M. Dugas, *Appl. Phys. Lett.* **69**, 705 (1996).
²⁷R. Proksch, G.D. Skidmore, E.D. Dahlberg, S. Foss, J.J. Schmidt, C. Merton, B. Walsh, and M. Dugas, *Appl. Phys. Lett.* **69**, 2599 (1996).
²⁸A. Hubert and R. Schäfer, *Magnetic Domains* (Springer Verlag, Berlin, 1998).
²⁹C. Kittel, *Phys. Rev.* **70**, 965 (1946).
³⁰C.C.H. Lo, J.E. Snyder, J. Leib, R. Chen, B. Kriegermeier-Sutton, M.J. Kramer, D.C. Jiles, and M.T. Kief, *J. Appl. Phys.* **89**, 2868 (2001).
³¹ $K(k) = \int_0^{\pi/2} \frac{d\psi}{\sqrt{1-k^2 \sin^2 \psi}}$, $E(k) = \int_0^{\pi/2} \sqrt{1-k^2 \sin^2 \psi} d\psi$.
³²H.J.G. Draaisma, F.J.A. den Broeder, and W.J.M. de Jonge, *J. Magn. Magn. Mater.* **66**, 351 (1987).
³³F.J.A. den Broeder, D. Kuiper, A.P. van de Mosselaer, and W. Hoving, *Phys. Rev. Lett.* **60**, 2769 (1988).
³⁴T. Garel and S. Doniach, *Phys. Rev. B* **26**, 325 (1982).
³⁵M. Seul and R. Wolfe, *Phys. Rev. Lett.* **68**, 2460 (1992).
³⁶A.B. Kashuba and V.L. Pokrovsky, *Phys. Rev. B* **48**, 10 335 (1993).

- ³⁷H. Westfahl, J. Schmalian, and P.G. Wolynes, Phys. Rev. B **64**, 174203 (2001).
- ³⁸S. Hameed, P. Talagala, R. Naik, L.E. Wenger, V.M. Naik, and R. Proksch, Phys. Rev. B **64**, 184406 (2001).
- ³⁹G. Bochi, H.J. Hug, D.I. Paul, B. Stiefel, A. Moser, I. Parashikov, H.-J. Güntherodt, and R.C. O'Handley, Phys. Rev. Lett. **75**, 1839 (1995).
- ⁴⁰H.J.G Draaisma and W.J.M de Jonge, J. Appl. Phys. **62**, 3318 (1987).